A semi-analytical model of a discretely supported railway track

Jiawei Wang, David Thompson, Giacomo Squicciarini

Institute of Sound and Vibration Research, University of Southampton, Southampton SO17 1BJ, UK

Abstract: The dynamic behaviour of railway track plays an important role in the generation of rolling noise as well as the development of rail corrugation. A semi-analytical model is presented that includes vertical, lateral and axial dynamics and takes account of the discrete supports provided by the sleepers. The rail is represented by a semi-analytical beam model that includes vertical and lateral bending, extension and torsion, with warping and shear-centre eccentricity. A receptance-coupling method is used to couple the rails, through damped springs that represent the rail pads, with a finite number of flexible sleepers that are in turn supported on an elastic foundation. The model also accounts for the coupling between the two rails through the sleepers. Results are presented in terms of the point mobilities in different directions, including the vertical-lateral cross mobility, as well as the track decay rates, and the results are validated by comparison with measurements. The inclusion of torsion and warping is shown to have a significant effect on the lateral rail mobility, leading to better agreement with the measured results. The response on one rail due to excitation on the other rail is also explored and the results agree well with the measurements. It is found that the coupling between the two rails has only a limited effect on the resultant track response.

Keywords: Discretely supported track; Railway track dynamics; Vertical/lateral coupling; Flexible sleepers; Coupling between rails

1   Introduction

The dynamic behaviour of railway track plays an important role in the generation of rolling noise [1, 2, 3] as well as in the development of rail corrugation [4, 5, 6]. Appropriate models can be used not only to understand the mechanisms of rolling noise generation and corrugation development, but also to study suitable mitigation strategies. Such models should contain sufficient detail to represent the physical phenomena whilst avoiding excessive computation

times. A typical ballasted track consists of two rails, attached through rail pads to discrete sleepers that are in turn supported by the ballast. Many authors have used analytical beam models to study the vertical dynamics of the track and have commonly assumed an equivalent continuous support, e.g. [2, 7]. Much less attention has been paid to the lateral vibration or the coupling between the vertical and lateral directions [8]. Thompson et al. [3, 7] used a Timoshenko beam on a two-layer foundation to model both the vertical and lateral track dynamics and estimated the cross receptance between vertical and lateral directions from the geometrical average of the vertical and lateral receptances, using an empirical scaling factor.

The effect of the discrete nature of the support is most evident around the 'pinned-pinned' frequency, at which the sleeper spacing corresponds to half a bending wavelength in the rail. Grassie et al. [9] proposed a discretely supported track model, in which the sleepers were represented by lumped masses and the rail pads and ballast by damped springs. Compared with the continuously supported track model, a resonance peak was found at the pinned-pinned frequency for excitation between sleepers and a corresponding dip for excitation above a sleeper. Similar models were also applied to lateral [10] and longitudinal vibration [11].

Heckl [12] introduced a discretely supported track model in which an infinite Timoshenko beam was used to represent the vertical vibration of the rail, while a finite number of discrete supports were considered, which were replaced by point reaction forces acting on the infinite rail. Heckl [13] later developed a model of a Timoshenko beam, including torsional and extensional waves, with an infinite number of periodically spaced supports, and studied coupled waves in all three directions.

At higher frequencies cross-sectional deformation of the rail becomes important [1]. Wu and Thompson [14, 15] developed multiple-beam models to explore the vertical and lateral response including an approximation for cross-sectional deformation. Discretely supported versions of the models were also developed [14, 16]. Bhaskar et al. [17] introduced an analytical model that accounted for the lateral and torsional motion of the rail. The rail head was represented as a beam, while the rail web and foot were represented by three plates, one for the web and one for the foot on each side of the web.

Betgen et al. [18] showed, in comparison with measurements and a detailed finite element (FE) model, that the analytical beam models of [3] were unable to capture some key characteristics of the response, particularly the vertical-lateral cross mobility and track decay rates. The lateral position of the vertical excitation force was shown to have a great influence on the cross mobility.

2

Kostovasilis et al. [19] introduced a semi-analytical rail model which accounts for vertical and lateral bending, extension and torsion. Although cross-section deformation was not considered, the inclusion of torsion and corrections for shear centre eccentricity and warping improved the lateral response of the track. In comparison with measurements and the results from a waveguide FE model, good agreement was found for the vertical and lateral mobilities for frequencies up to 3 kHz and for the decay rates up to 2 kHz. There was also generally good agreement between measurements and calculations for the cross mobility.

Numerical methods can be used to include the effects of cross-sectional deformation in the track response. Thompson [20] modelled a short slice of rail on a continuous support using finite elements and used periodic structure theory to obtain the dispersion relationship and receptances. Knothe et al. [21] used the finite strip method, in which only the cross-section of the rail is discretised, to study the free wave propagation in a rail. Similarly, Ryue et al. [22] determined the waves propagating in a continuously supported rail up to 80 kHz using the waveguide FE method (also known as the 2.5D FE method). Nilsson et al. [23] used the waveguide FE and boundary element methods to calculate the vibration and sound radiation of an infinite continuously supported rail. A similar approach has been used for a continuously supported rail with multiple layer support [24].

To include discrete supports, Gry [25] used a method similar to the finite strip method to derive the vibrational response in terms of a sum of waves. Zhang et al. [26] established a model of a discretely supported track by combining the 2.5D FE method for the rail and Heckl's receptance-coupling method [12] for discrete supports. The overall track mobilities and decay rates agreed well with measurements.

Although many models represent the sleepers as a lumped mass, Grassie and Cox [27] modelled the sleepers as finite uniform Timoshenko beams supported by an elastic layer, while Nielson and Igeland [28] used beam finite elements to account also for the variable cross-section. Grassie [29] proposed a simple uniform Timoshenko beam model for a freely suspended sleeper and a similar model was subsequently used in [3, 26] with the addition of an elastic layer to represent the ballast.

In almost all published models of track vibration, either a single rail is considered, or symmetry is applied at the track centre. Betgen et al. [18] and Oregui et al. [30] used detailed FE models of a long section of track, including both rails, but the effect of the coupling through the sleeper was not investigated.

In the present work, a semi-analytical model of a discretely supported track is introduced with the aim of better predicting the track dynamics without resorting to fully numerical models.

Infinitely long rails are modelled using the semi-analytical approach of Kostovasilis et al. [19], which considers vertical and lateral bending, torsion and warping, vertical/lateral coupling and axial dynamics. The present work develops the approach of Kostovasilis [19, 31] by including discrete supports, flexible sleepers and coupling with a second rail. The rails are connected to a finite number of sleepers through damped springs. The sleepers are represented by flexible beams, supported on a viscoelastic layer representing the ballast. The receptance-coupling method [12, 26] is used to couple the rails to the sleepers. The point mobilities and track decay rates are obtained using this model and compared with results from measurements. The inclusion of torsion and warping was introduced by Kostovasilis et al. [19] but their effect on the lateral track response is investigated here. Finally, the response of one rail to excitation on the other is presented.

2   Modelling a discretely supported track

Various methods are available to model the vibration of a track with discrete supports, Fig. 1(a). The approach applied here is based on the advanced beam model of Kostovasilis et al. that includes bending, torsion, warping and extension [19]. This beam model is implemented in the discrete support framework proposed by Heckl [12]. This latter approach replaces the discrete rail supports by a set of point forces acting on an infinite free rail. To implement this method, the point and transfer receptances of the free rail are required, as well as the receptances of the sleepers and rail pads. In the current model, two rails are coupled to flexible sleepers, as shown in Fig. 1(b).
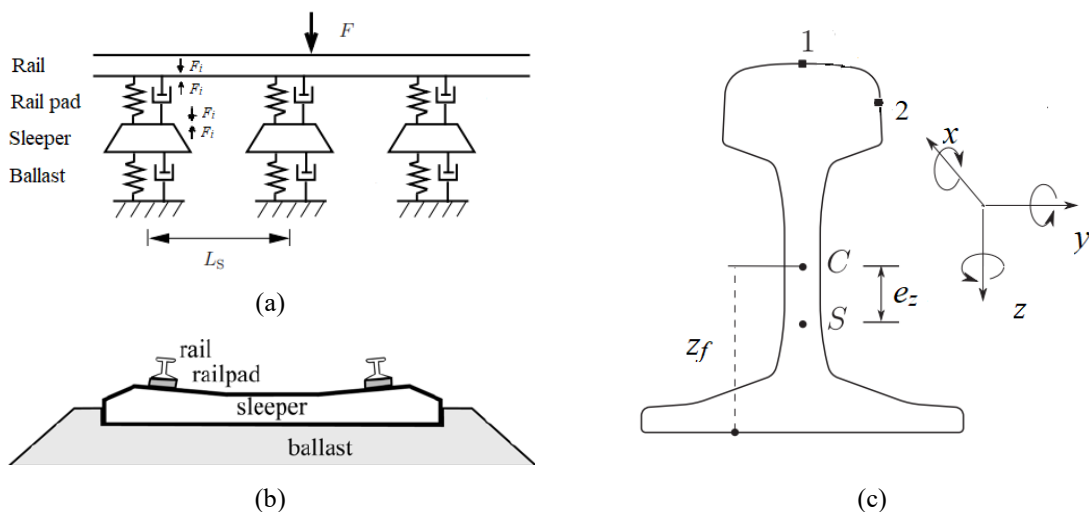
Fig. 1 (a) Side view of track model, where L_s is the sleeper spacing; F_i is the force transmitted at the ith discrete support; (b) front view of track model, showing two rails connected to the sleeper; (c) the coordinate system, shear centre S and centroid C of the rail cross-section

4

2.1 Semi-analytical rail model

For a Vignole rail, e.g. 60E1, as used on mainline tracks, the rail cross-section is symmetric about the vertical mid-plane but is asymmetric about the horizontal mid-plane. Consequently, as shown in Fig. 1(c), the shear centre, through which the shear forces are considered to act, is not coincident with the centroid through which the inertial forces are considered to act. This introduces coupling between lateral bending and torsion.

To represent the free rail, the semi-analytical beam model developed by Kostovasilis et al. [19] is used. This is briefly introduced here. The model uses Timoshenko beam theory for bending in the vertical and lateral directions, as well as rod theory in extension. It also includes non-uniform torsion and accounts for the shear-centre eccentricity.

Assuming harmonic response in both space and time, with circular frequency ω and complex wavenumber ξ, the vibration at the centroid can be written as:

$$\mathbf{U} = \widetilde{\mathbf{U}} e^{i\omega t} e^{-i\xi x} \tag{1}$$

in which $\widetilde{\mathbf{U}} = \left[\widetilde{U}_x, \widetilde{U}_y, \widetilde{U}_z, \widetilde{\theta}_x, \widetilde{\theta}_y, \widetilde{\theta}_z, \widetilde{U}_w\right]^T$ is a vector of complex amplitudes, consisting of seven components of vibration (three displacements, three rotations and warping) at the centroid. $\mathbf{F}$ is the corresponding vector of the external forces and moments, which is assumed to act at $x = 0$, and is given as $\mathbf{F} = \widetilde{\mathbf{F}} e^{i\omega t} \delta(x)$ with $\widetilde{\mathbf{F}}$ the vector of the corresponding amplitudes in the wavenumber domain.

The equation of motion can be written in the frequency-wavenumber domain as [19]:

$$\{(\mathbf{K}_0 - \omega^2 \mathbf{M}) - i\xi \mathbf{K}_1 - \xi^2 \mathbf{K}_2\}\widetilde{\mathbf{U}} = \widetilde{\mathbf{F}} \tag{2}$$

where $\mathbf{K}_0$ is the stiffness matrix, $\mathbf{K}_1$ and $\mathbf{K}_2$ contain stiffness terms related to the first and second derivatives in the x direction and $\mathbf{M}$ is the mass matrix. The matrices in Eq. (2) are given in [19].

An external force at the excitation point (on the rail head or rail foot) can be applied in each of three directions. For a vertical distance z_e between the excitation point and the centroid, and a lateral distance y_e, the external force vector for forces $\widetilde{F}_x$, $\widetilde{F}_y$, and $\widetilde{F}_z$ is given as

$$\widetilde{\mathbf{F}} = \left[\widetilde{F}_x, \widetilde{F}_y, \widetilde{F}_z, (z_e\widetilde{F}_y - y_e\widetilde{F}_z), z_e\widetilde{F}_x, y_e\widetilde{F}_x, 0\right]^T \tag{3}$$

Moment excitation can also be applied. Moreover, because of the lateral distance y_r and vertical distance z_r between an arbitrary response point and the centroid, the responses obtained at the centroid need to be multiplied with a transformation matrix, which is given in [19], to give the response at the rail head or foot.

To solve Eq. (2), the case of free vibration, $\tilde{\mathbf{F}} = \mathbf{0}$, is first considered. This is a dual (non-linear) eigenvalue problem in ω and complex wavenumber ξ. Eq. (2) is rewritten as:

$$\mathbf{A}_1 \mathbf{v} + i\xi \mathbf{A}_2 \mathbf{v} = \mathbf{0} \tag{4}$$

where $\mathbf{v} = [\tilde{\mathbf{U}} \quad i\xi\tilde{\mathbf{U}}]^T$,

$$\mathbf{A}_1 = \begin{bmatrix} \mathbf{K}_0 - \omega^2 \mathbf{M} & -\mathbf{K}_1 \\ \mathbf{0}_{7\times7} & \mathbf{I}_{7\times7} \end{bmatrix} \tag{5}$$

and

$$\mathbf{A}_2 = \begin{bmatrix} \mathbf{0}_{7\times7} & \mathbf{K}_2 \\ -\mathbf{I}_{7\times7} & \mathbf{0}_{7\times7} \end{bmatrix} \tag{6}$$

Eq. (4) can be solved to give complex wavenumbers ξ_n, which occur in pairs $(\pm\xi_n)$, and the corresponding (1×7) left eigenvectors $\mathbf{U}_{nL}$, and (7×1) right eigenvectors, $\mathbf{U}_{nR}$, for each frequency. To obtain the response in the spatial domain, the inverse Fourier transform is used:

$$\mathbf{U}(x) = \frac{1}{2\pi} \int_{-\infty}^{\infty} \tilde{\mathbf{U}} e^{-i\xi x} d\xi \tag{7}$$

The integration is performed using the contour integration approach. For $x \geq 0$, the integral solution is given by the sum of the residues of the poles lying in the lower half plane, $\text{Im}(\xi_n) < 0$. These poles are the free wavenumber solutions ξ_n obtained above. The solution in the spatial domain is obtained as:

$$\mathbf{U}(x) = -i \sum_{\text{Im}(\xi_n)<0} \frac{\mathbf{U}_{nL}\tilde{\mathbf{F}}}{\mathbf{U}_{nL}\mathbf{A}'(\xi_n)\mathbf{U}_{nR}} \mathbf{U}_{nR} e^{-i\xi_n x} \quad \text{for } x \geq 0 \tag{8}$$

where $\mathbf{A}'(\xi_n) = -2\xi_n\mathbf{K}_2 - i\mathbf{K}_1$ is the derivative of the dynamic stiffness matrix and x is the longitudinal distance between excitation and response points.

2.2 Rail pad model

The rail pad connects the rail to the sleeper dynamically. Measurements have shown that the rail pad damping is well approximated by using a dynamic stiffness with a constant loss factor [1].

Each rail pad is considered here as a single damped spring in each direction. The dynamic stiffness of the rail pads has six components. k_x, k_y, k_z are used to represent the longitudinal, lateral and vertical stiffness. For simplicity, the rotational stiffnesses are estimated from the translational stiffnesses, assuming a homogeneous material for the pad:

$$k_{xr} = k_{yr} = \frac{l_p^2}{12} k_z \tag{9}$$

$$k_{zr} = \frac{l_p^2}{12} k_x + \frac{l_p^2}{12} k_y \qquad (10)$$

in which it is assumed that the pad is square with length l_p. Consequently, the pad stiffnesses in longitudinal and lateral directions are assumed to be identical.

2.3 Sleeper model

The sleeper is represented as a finite uniform Timoshenko beam [29] of length *L*, and is assumed to be supported on a continuous viscoelastic foundation which represents the ballast. The modelling approach for the sleeper is similar to that described in Ref. [1], in which the receptance is obtained from a wave approach. As the sleeper cross-section is symmetric, the sleeper model can be seen as two separate models, one involving the axial sleeper response and vertical sleeper bending, and the other involving the torsional response and lateral sleeper bending. Note that the axial direction of the sleeper is coincident with the lateral direction of the rail, while the lateral direction of the sleeper is coincident with the axial direction of the rail. Thus, the receptance of the sleeper needs to be transformed to match the coordinate system of the rail when assembling the track model.

In the sleeper model, there is coupling between its vertical and axial responses and between lateral and torsional responses; this originates from the foundation eccentricity, in which the ballast stiffness is assumed to act at the bottom of the sleeper. Finally, appropriate boundary conditions are applied to accommodate the finite length of the sleeper. The detailed modelling process is presented in [31].

Using the parameters listed in Table 1, the point mobilities (velocities for a unit force) of the sleeper at one rail seat and the transfer mobilities from one side to the other are obtained, as shown in Fig. 2. Results are shown for all three translational directions. In all three directions, there is a highly damped resonance at around 100 Hz, in which the sleeper mass bounces on the ballast stiffness. A series of resonances of the flexible sleeper are seen above 400 Hz in the vertical and lateral directions. The first extensional mode occurs at 1 kHz. Compared with the point mobilities, the transfer mobilities in vertical and lateral directions are lower, whereas in the axial direction they are of similar magnitude.

Table 1 Parameters used for the calculations

Sleeper parameters	Vertical	Axial to sleeper	Lateral to sleeper
Equivalent dimensions, m	$h = 0.185$	$L = 2.5$	$w = 0.245$
Second moment of area, m^4	$I_{p,z} = 1.27 \times 10^{-4}$	–	$I_{p,y} = 2.24 \times 10^{-4}$
Shear coefficient	$\kappa_z = 0.83$	–	$\kappa_y = 0.83$
Sleeper spacing, m	0.65		
Young's modulus E, GPa	57.0		
Density ρ, kg/m^3	2648		
Poisson's ratio v	0.2		
Damping loss factor η	0.0083		
Polar moment of area I_p, m^4	3.51×10^{-4}		
Torsional constant J, m^4	2.70×10^{-4}		
Ballast parameters **(per unit length along the sleeper)**			
Ballast stiffness, MN/m^2	68	58	58
Ballast damping, kNs/m^2	82	68	68
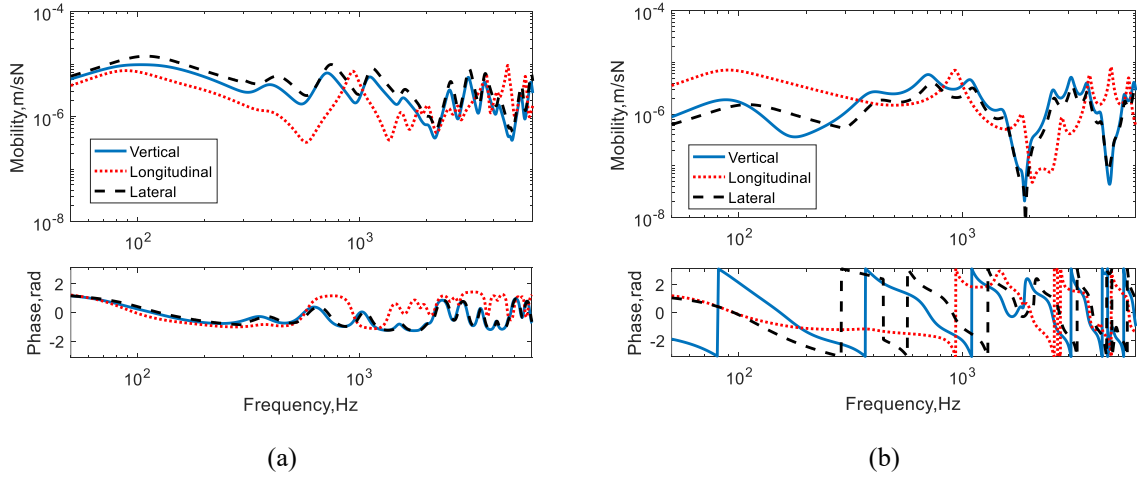
Fig. 2 Mobilities of the sleeper; the directions identified correspond to local sleeper coordinates. (a) Point mobilities at one rail seat; (b) transfer mobilities to the other rail seat

2.4 Receptance-coupling approach

Following the method of Refs [12, 26], the infinite rail is coupled to a finite number of sleepers through the rail pads, see Fig. 1(a). This approach is extended here to use the beam model of Kostovasilis et al. [19] and to include both rails. The rail pads are assumed to be massless so that the same forces act on both the rail and sleepers but in opposite directions. The two rails are denoted left and right and it is assumed that the external force F_e is applied to the left rail.

The vectors of displacement on the rail foot of the left and right rail at the connection points with the rail pads (three displacements and three rotations) are denoted $\mathbf{u}_{rL}$ and $\mathbf{u}_{rR}$. The corresponding displacement vectors on the sleepers are denoted $\mathbf{u}_{sL}$ and $\mathbf{u}_{sR}$. If there are N sleepers, these vectors have dimension $6N{\times}1$. These are combined into $12N{\times}1$ vectors $\mathbf{u}_r = [\mathbf{u}_{rL}{}^{\mathrm{T}} \; \mathbf{u}_{rR}{}^{\mathrm{T}}]^{\mathrm{T}}$ and $\mathbf{u}_s = [\mathbf{u}_{sL}{}^{\mathrm{T}} \; \mathbf{u}_{sR}{}^{\mathrm{T}}]^{\mathrm{T}}$. $\mathbf{F}_L$ and $\mathbf{F}_R$ are the corresponding vectors of interaction forces at the left and right connection points, which are combined into a single force vector $\mathbf{F} = \begin{bmatrix} \mathbf{F}_L{}^{\mathrm{T}} & \mathbf{F}_R{}^{\mathrm{T}} \end{bmatrix}^{\mathrm{T}}$. The sleepers are represented by $12N{\times}12N$ matrices of receptances (displacement for a unit force)

$$\boldsymbol{\alpha}^s = \begin{bmatrix} \boldsymbol{\alpha}_L^S & \boldsymbol{\alpha}_{LR}^S \\ \boldsymbol{\alpha}_{RL}^S & \boldsymbol{\alpha}_R^S \end{bmatrix} \tag{11}$$

in which $\boldsymbol{\alpha}_L^S$ is the matrix of receptances of the sleepers at the points connected to the left rail, which are given by

$$\boldsymbol{\alpha}_L^S = \begin{bmatrix} \ddots & & 0 \\ & \boldsymbol{\alpha}_{L,i}^S & \\ 0 & & \ddots \end{bmatrix} \tag{12}$$

where $\boldsymbol{\alpha}_{L,i}^S$ is the $6{\times}6$ receptance matrix for a single sleeper. Similarly, $\boldsymbol{\alpha}_R^S$ are the matrices of receptances of the sleeper at the points connected to the right rail and $\boldsymbol{\alpha}_{LR}^S$, $\boldsymbol{\alpha}_{RL}^S$ contain the transfer receptances between the left and right connection points.

Similarly, the connection points on the left rail are described by the matrix $\boldsymbol{\alpha}_L^r$ and those on the right rail by $\boldsymbol{\alpha}_R^r$, giving a combined receptance matrix for both rails as:

$$\boldsymbol{\alpha}^r = \begin{bmatrix} \boldsymbol{\alpha}_L^r & \mathbf{0} \\ \mathbf{0} & \boldsymbol{\alpha}_R^r \end{bmatrix} \tag{13}$$

The rail pads are represented by a $12N{\times}12N$ diagonal matrix of receptances $\boldsymbol{\alpha}^p$.

Considering all the connection points on both rails, the equations of motion can be written in matrix form as:

$$\mathbf{u}_r = \boldsymbol{\alpha}_e^r F_e - \boldsymbol{\alpha}^r \mathbf{F} \tag{14}$$

$$\mathbf{u}_r - \mathbf{u}_s = \boldsymbol{\alpha}^p \mathbf{F} \tag{15}$$

$$\mathbf{u}_s = \boldsymbol{\alpha}^s \mathbf{F} \tag{16}$$

where $\boldsymbol{\alpha}_e^r$ is the vector of transfer receptances of the rail from the external force F_e at a position on the left rail head to the responses at the connection points (for positions on the right rail it contains zeros). Combining Eq. (15) and (16) gives

$$\mathbf{u}_r = (\boldsymbol{\alpha}^p + \boldsymbol{\alpha}^s)\mathbf{F} \tag{17}$$

Substituting this into Eq. (14) and rearranging, the rail displacements at the connection points can be obtained as:

$$\mathbf{u}_r = (\mathbf{I} + \boldsymbol{\alpha}^r(\boldsymbol{\alpha}^p + \boldsymbol{\alpha}^s)^{-1})^{-1}\boldsymbol{\alpha}_e^r F_e \tag{18}$$

where $\mathbf{I}$ is the unit matrix.

The rail displacements $\mathbf{u}_r$ are used to obtain the interaction forces $\mathbf{F}$ by inverting Eq. (17). The displacement at an arbitrary point k on the left rail can finally be calculated as

$$u_{L,k}^r = \alpha_{L,ke}^r F_e - \boldsymbol{\alpha}_{L,k}^r \mathbf{F}_L \tag{19}$$

where $\boldsymbol{\alpha}_{L,k}^r$ is a vector of transfer receptances of the free rail, giving the response at the point k to a unit force at each rail pad location on the rail foot; $\alpha_{L,ke}^r$ is the transfer receptance of the free rail from the external force F_e to the response point k. By applying a unit force on the rail head, in each direction in turn, the responses $u_{L,k}^r$ correspond to the receptances of the assembled track. They can be expressed as mobilities by using $Y = i\omega u_k^r$. Similarly, the responses at an arbitrary point k on the right rail to excitation on the left rail are given by

$$u_{R,k}^r = -\boldsymbol{\alpha}_{R,k}^r \mathbf{F}_R \tag{20}$$

A similar model can be used with a single rail, in which case reduced matrices $\boldsymbol{\alpha}^r = \boldsymbol{\alpha}_L^r$, $\boldsymbol{\alpha}^p = \boldsymbol{\alpha}_L^p$ and $\boldsymbol{\alpha}^s = \boldsymbol{\alpha}_L^s$ are used.

3 Track response results

3.1 Point and transfer mobility

The receptance-coupling method described in Section 2.4 is applied to obtain the response of the discretely supported railway track. At this stage only a single rail is included. To ensure the waves generated are sufficiently attenuated at the ends of the finite supported region, 121 rail supports are included in the longitudinal direction. The rail type is CEN 60E1. Table 2 lists the parameters used for the rails and rail pads, which are mainly derived from [19], although the rail pad properties are adjusted to match the measurements described below. The parameters for the sleepers and ballast were given in Table 1. The frequency range used in the calculations is from 50 Hz to 6000 Hz, with a constant spacing with 1 Hz interval.

Table 2 Parameters used for the calculations

Rail parameters	Vertical	Lateral	Longitudinal
Rail bending stiffness, MNm^2	6.38	1.08	–
Shear coefficient	$\kappa_z = 0.393$	$\kappa_y = 0.538$	–
Rail loss factor	0.02	0.02	0.02
Young's modulus E, GPa	210		
Density ρ, kg/m^3	7850		
Rail mass per unit length, kg/m	60		
Poisson's ratio v	0.3		
Polar moment of area I_p, m^4	3.550×10^{-5}		
Torsional constant J, m^4	2.212×10^{-6}		
Warping constant I_w, m^6	2.161×10^{-8}		
Warping product moment of area, m^5	$I_{wy} = 0$	$I_{wz} = 1.6971 \times 10^{-7}$	–
Shear centre eccentricity, m	$e_z = 0.033$	$e_y = 0$	–
Rail pad parameters			
Pad stiffness, MN/m	300	40	40
Pad damping loss factor	0.25	0.25	0.25
Rail pad width l_p, m	–	0.150	0.150
Foot to centroid distance z_f, m	0.081	–	

For a vertical force, the excitation position is at the centre of the rail head (position 1 in Fig. 1(c)). Fig. 3 compares the calculated point mobilities of the track with results measured on a test track of length 32 m, for vertical excitation at mid-span between sleepers and directly above a sleeper. Very good agreement is obtained below 4 kHz. Pronounced differences can be seen between the results for the two excitation points, especially in the frequency range between 500 Hz and 2000 Hz. For the vertical mobility at mid-span, three obvious peaks can be identified. The first peak at 100 Hz corresponds to the resonance of the rail and sleeper mass on the vertical ballast stiffness, while the second peak at 470 Hz is the resonance of the rail mass on the vertical rail pad stiffness. There are also some oscillations due to the bending modes of the sleepers. The peak at 980 Hz is the vertical 'pinned-pinned' frequency; a dip appears just above this frequency in the mobility above the sleeper.
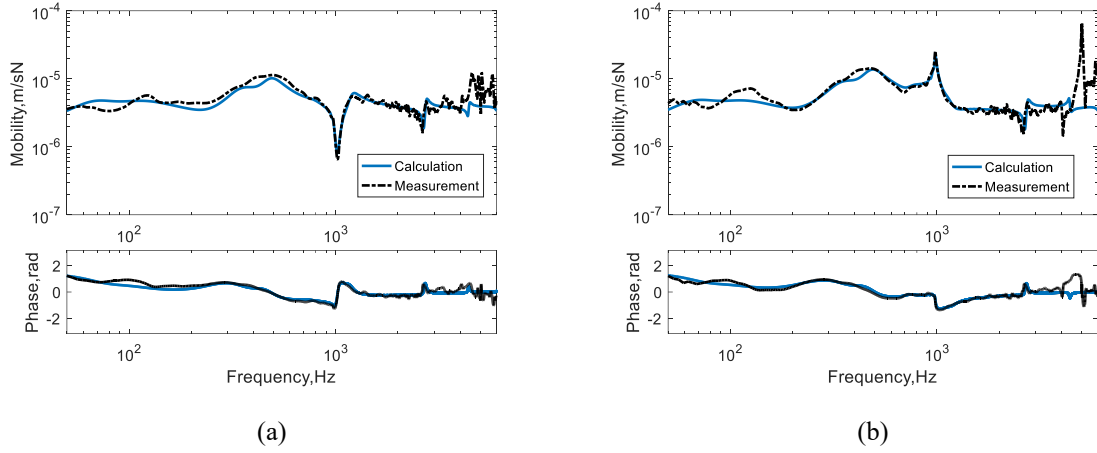
Fig. 3 Vertical point mobility of the track. (a) Above sleeper; (b) mid-span

For the lateral force, the excitation position is at the side of the rail head (position 2 in Fig. 1(c)). The lateral point mobility is shown in Fig. 4(a) and corresponding measured results in Fig. 4(b). A distinct peak can be observed in the lateral mobility at 140 Hz, corresponding to the resonance of the rail and sleeper mass on the lateral ballast stiffness. The peak at 470 Hz at mid-span is the lateral 'pinned-pinned' resonance and that at 670 Hz is the torsional 'pinned-pinned' resonance. Dips are found at these two frequencies in the mobility above the sleeper. The large oscillations in the measured results between 600 and 1500 Hz are due to the finite length of the test track, as there is a low decay rate in this frequency region. Apart from this, there is satisfactory agreement between measurements and calculations.
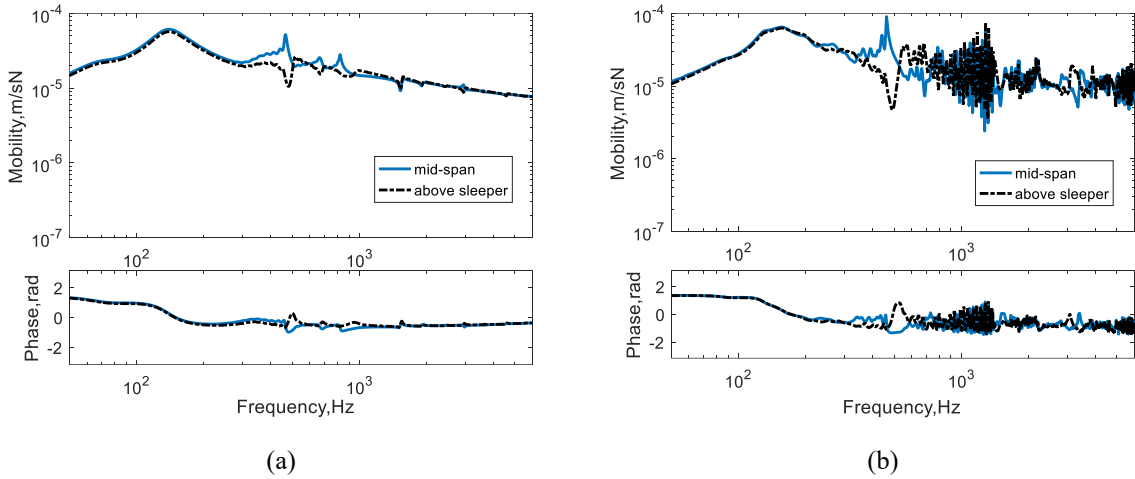
Fig. 4 Lateral point mobility of the track. (a) Predicted; (b) measured

Fig. 5(a) shows the predicted axial mobility at mid-span and above a sleeper for excitation at the centre of the rail head (position 1 in Fig. 1(c)). This rises to a peak at 200 Hz, which is the cut-on frequency of longitudinal waves. Above this frequency it is approximately flat, apart from the influence of the sleeper modes, until rising to a sharp peak at 5 kHz, which is the cut-on of the higher order wave of the Timoshenko beam.

Fig. 5(b) shows the predicted cross mobility (lateral response due to a vertical force) at a position with an offset of 10 mm from position 1 and at a position with an offset of 20 mm. For the offset of 10 mm, results are shown at mid-span and above a sleeper. The characteristics are very similar to the vertical and lateral point mobilities, with clear differences between mid-span and above a sleeper at the pinned-pinned resonances. For the larger offset, the magnitude of the cross mobility increases at all frequencies.

(a)

(b)
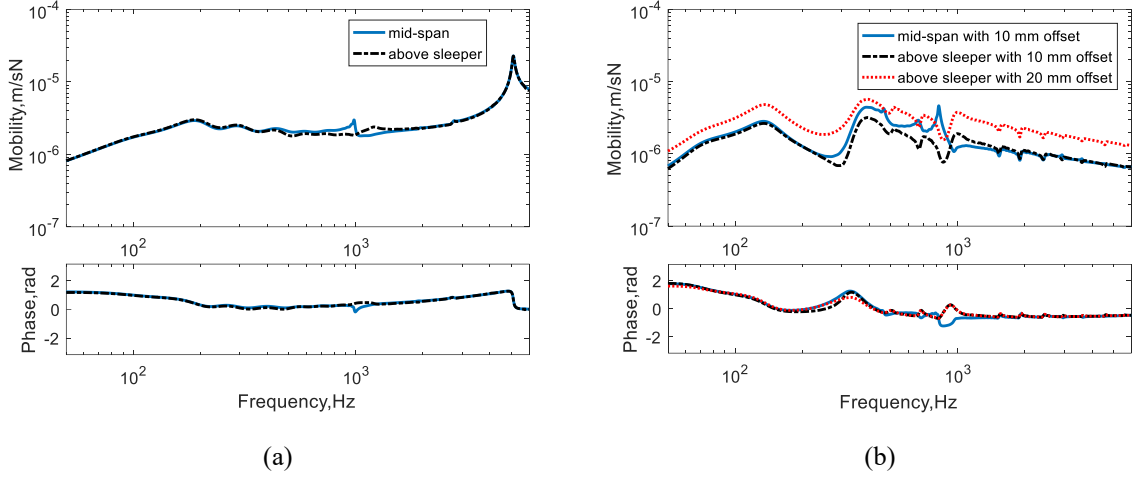
Fig. 5 Predicted mobility of the track excited at different positions. (a) Axial mobility; (b) vertical-lateral cross mobility

3.2 Decay rate

The track decay rate is determined from the transfer mobilities at different positions along the rail [32]. The overall decay rate in each one-third octave band is evaluated from predicted transfer mobilities according to the standard measurement method as [33]:

$$\Delta_{\text{tot}} = \frac{4.343}{\sum_{x=0}^{x_{\max}} \frac{|Y(x_n)|^2}{|Y(x_0)|^2} \delta x_n} \tag{21}$$

where $Y(x_n)$ is the transfer mobility in one-third octave bands at a distance x_n away from the excitation point, $Y(x_0)$ is the mobility at the excitation point and δx_n is the distance between the midpoints of each grid interval on either side of the location n.

The vertical decay rate is plotted in Fig. 6(a), and the lateral one in Fig. 6(b). These results are compared with measurements obtained on the same test track by Kostovasilis et al. [19].

13
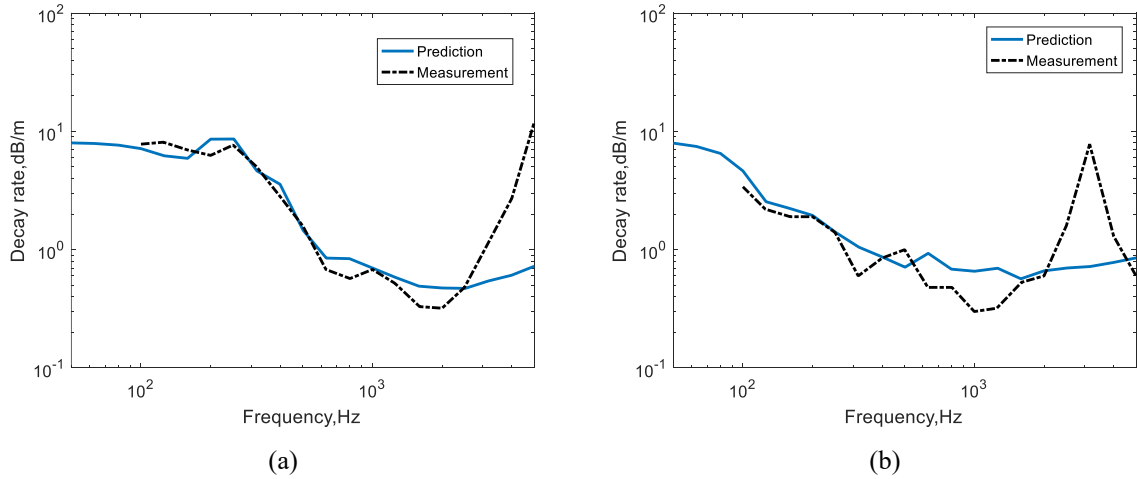
Fig. 6 Track decay rate compared with measured results from [19]. (a) Vertical direction; (b) lateral direction

Although the track was the same, the measured decay rates were obtained in warmer weather, which results in the rail pad being softer. Thus, the pad stiffnesses used in these calculations are adjusted to 120 MN/m for the vertical direction and 100 MN/m for the longitudinal and lateral directions, as given in [19]. At low frequencies, the vertical decay rate is high due to the blocking effect of the support stiffness. It drops at around the cut-on frequency of the rail vertical bending wave, which is around 300 Hz for these parameters. The lateral decay rate drops at a lower cut-on frequency. The agreement with measurements is very good up to 2 kHz, but at higher frequencies the measurements rise more rapidly due to cross-section deformation of the rail, which is not included in the model.

3.3 Effect of torsion and warping on the track response

The beam model used includes the effects of torsion and warping on the lateral responses [19]. To investigate their effects, results are obtained from the current model with and without torsion and warping. The track parameters from Table 1 are used and the excitation and response points are the same as considered above.

14
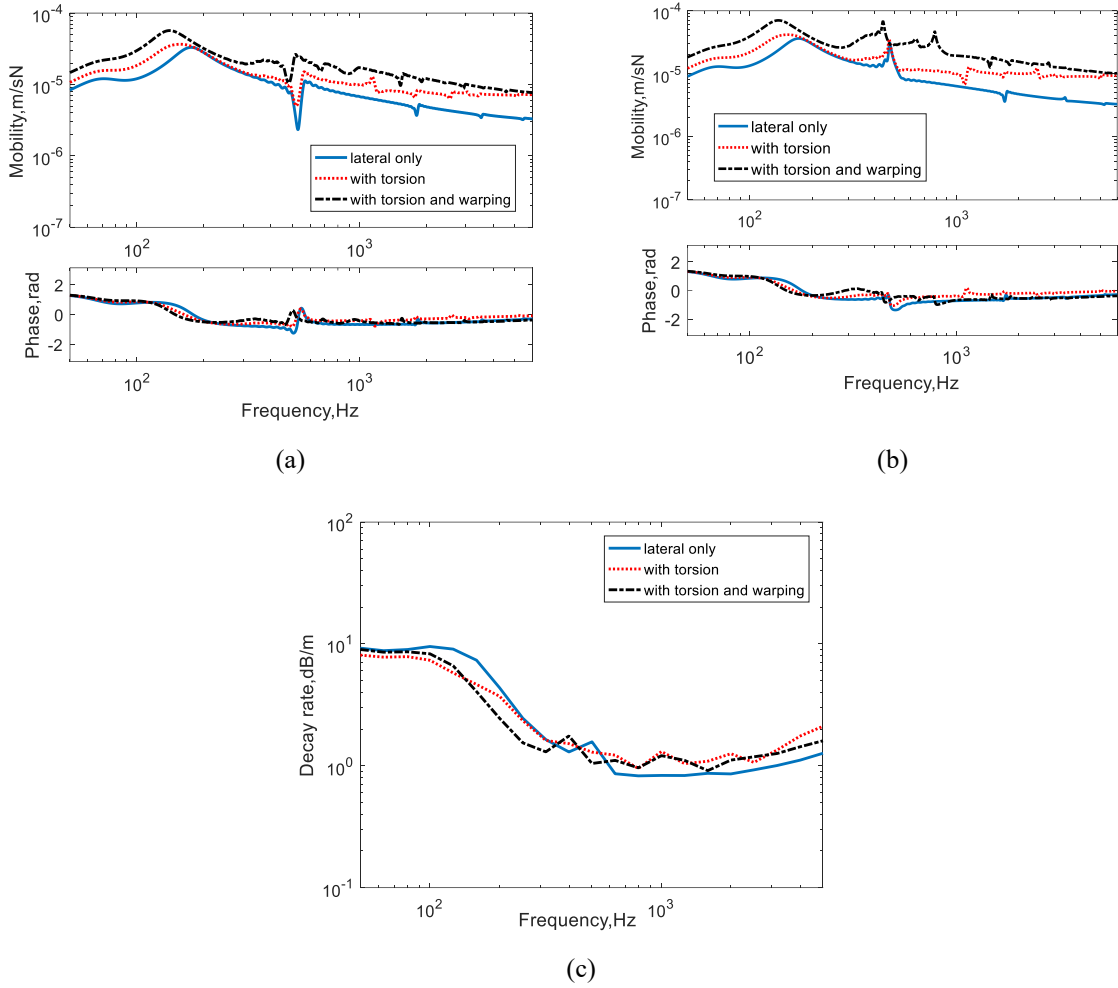
Fig. 7 Lateral results with or without torsion and warping. (a) Lateral point mobility above a sleeper, (b) Lateral point mobility at mid-span, (c) lateral track decay rate

The vertical point mobility and decay rate are unaffected by the inclusion of torsion and warping, so are not shown here. Fig. 7(a-b) shows the lateral point mobility above a sleeper and at mid-span, Fig. 7(c) shows the corresponding track decay rate. The inclusion of torsion and warping both have significant effects on the lateral response over the whole frequency range. The inclusion of torsion lowers the cut-on frequency of the lateral wave from 200 Hz to 150 Hz, which can be seen in both the mobility and the decay rate. The inclusion of warping then leads to a further increase in the magnitude of the mobility. The dip related to the lateral pinned-pinned resonance can be found even when only lateral bending is considered but the one related to the rotational pinned-pinned resonance is only found when warping is introduced.

3.4 Transfer mobility under excitation on the other rail

The model is now used to predict the response of the right rail to a force on the left rail. The same parameters are used as shown in Table 1. For the vertical direction, the excitation is at position 1 on the left rail and the response is at position 1 on the right rail. For the lateral

direction, the excitation is at position 2 on the left rail head and response is at position 2 on the right rail head.

Fig. 8 compares the transfer mobility with the point mobility for both vertical and lateral directions for excitation above a sleeper. The magnitudes of the point and transfer mobilities have a roughly constant difference at low frequency but the difference increases at high frequency. Nevertheless, there are some narrow frequency regions where the difference between point and transfer mobilities is rather small, for example around 400 Hz and 1 kHz for the vertical direction.

In Fig. 8 the predicted transfer mobility between the two rails is also compared with the corresponding measured results obtained on the test track. Good agreement can be seen between the measured and calculated mobilities. As the transfer mobility between the two rails is much lower than the point mobility, the coupling between the two rails is found to have little effect on the track mobilities on the excited rail or on the track decay rates.

(a)   (b)
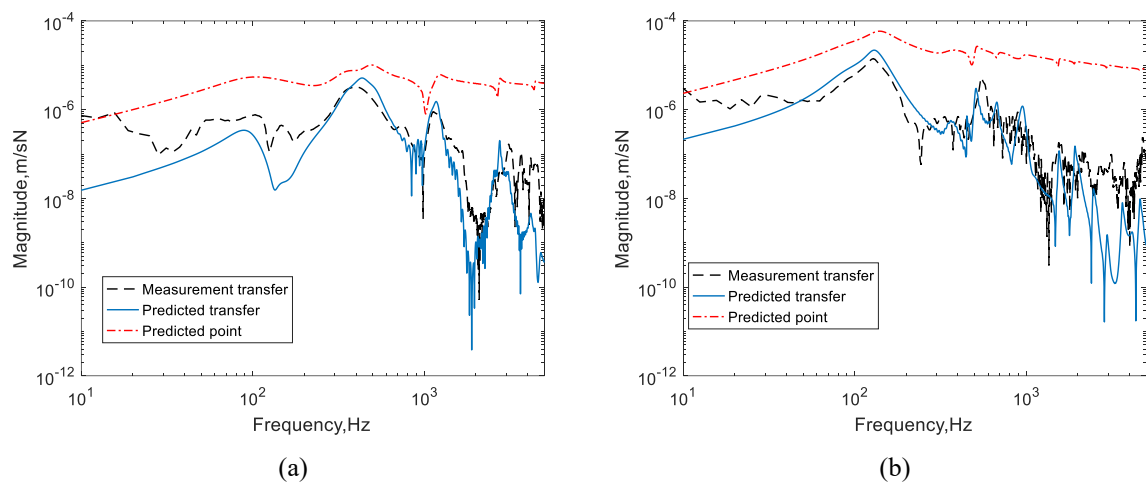
Fig. 8 Comparison of the predicted transfer mobility between two rails with the measurement and with the predicted point mobility, all results for excitation above a sleeper. (a) Vertical direction; (b) lateral direction.

4   Conclusions

A model of a discretely supported track is developed, which accounts for vertical and lateral bending, extension and torsion, with warping and shear-centre eccentricity. Coupling between the two rails is also included. The point mobilities in different directions are compared with measurements and found to show good agreement. The track decay rates are also investigated and found to agree well with measurements up to 2 kHz. The vertical-lateral cross mobility is shown to depend on the lateral offset of the vertical forcing point.

The inclusion of torsion and warping in the rail model has a significant effect on the lateral track mobility. The cut-on frequency of the lateral wave and the overall response amplitude are

both modified, and the lateral mobility shows better agreement with measurements when these effects are included.

The effect of coupling between the two rails connected through the sleepers is also investigated. The transfer mobilities between the two rails agree well with measurements. They are found to be much smaller than the point mobilities apart from some narrow frequency regions. Consequently, that the track mobilities on the excited rail and the track decay rates are largely unaffected by the coupling with the second rail.

Declaration of conflicting interests

The author declares that there are no potential conflicts of interest with respect to the research, authorship, and/or publication of this article.

References

1   D.J. Thompson. *Railway Noise and Vibration: Mechanisms, Modelling and Means of Control*. Elsevier, Oxford, UK, 2009.

2   P.J. Remington. Wheel/rail rolling noise I: theoretical analysis. *Journal of Acoustical Society of America* 1987; 81: 1805-1823.

3   D.J. Thompson, B. Hemsworth, N. Vincent. Experimental validation of the TWINS prediction program for rolling noise, Part 1: description of the model and method. *Journal of Sound and Vibration* 1996; 193: 123-135.

4   A. Igeland. Railhead corrugation growth explained by dynamic interaction between track and bogie wheelsets. *Proceedings of the Institution of Mechanical Engineers, Part F: Journal of Rail and Rapid Transit* 1996; 210: 11-20.

5   O. Oyarzabal, J. Gomez, J. Santamaria, E.G. Vadillo. Dynamic optimization of track components to minimize rail corrugation. *Journal of Sound and Vibration* 2009; 319: 904–917.

6   P.T. Torstensson, M. Schilke, Rail corrugation growth on small radius curves – Measurements and validation of a numerical prediction model. *Wear* 2013; 303: 381-396.

7   D.J. Thompson, N. Vincent. Track dynamic behaviour at high frequencies. Part 1: theoretical models and laboratory measurements. *Vehicle System Dynamics* 1995; 24 Supp: 86-99.

8   K.L. Knothe, S.L. Grassie. Modelling of railway track and vehicle/track interaction at high frequencies. *Vehicle System Dynamics* 1993; 22: 209-262.

9   S.L. Grassie, R.W. Gregory, D. Harrison, K.L. Johnson. The dynamic response of railway track to high frequency vertical excitation. *Journal of Mechanical Engineering Science* 1982; 24: 77–90.

10 S.L. Grassie, R.W. Gregory, K.L. Johnson. The dynamic response of railway track to high frequency lateral excitation. *Journal of Mechanical Engineering Science* 1982; 24: 91–95.

11 S.L. Grassie, R.W. Gregory, K.L. Johnson. The dynamic response of railway track to high frequency longitudinal excitation. *Journal of Mechanical Engineering Science* 1982; 24: 97–102.

12 M.A. Heckl. Railway noise - Can random sleeper spacings help? *Acustica* 1995; 81: 559-564.

13 M.A. Heckl. Coupled waves on a periodically supported Timoshenko beam. *Journal of Sound and Vibration* 2002; 252: 849-882.

14 T.X. Wu, D.J. Thompson. A double Timoshenko beam model for vertical vibration analysis of railway track at high frequencies. *Journal of Sound and Vibration* 1999; 224: 329-348.

15 T.X. Wu, D.J. Thompson. Analysis of lateral vibration behavior of railway track at high frequencies using a continuously supported multiple beam model. *Journal of Acoustical Society of America* 1999; 106: 1369–1376.

16 T.X. Wu, D.J. Thompson, Application of multiple beam model for lateral vibration analysis of a discretely supported rail at high frequencies. *Journal of the Acoustical Society of America* 2000; 108: 1341-1344.

17 A. Bhaskar, K.L. Johnson, G.D. Wood, J. Woodhouse. Wheel-rail dynamics with closely conformal contact. Part 1: dynamic modelling and stability analysis. *Proceedings of the Institution of Mechanical Engineers, Part F: Journal of Rail Rapid Transit* 1997; 211: 11–26.

18 B. Betgen, G. Squicciarini, D.J. Thompson. On the prediction of rail cross mobility and track decay rates using finite element models. In: *Proceedings of the 10th European Congress and Exposition on Noise Control Engineering (EURONOISE2015)*, Maastricht, Netherlands, 2015, pp.2019–2024.

19 D. Kostovasilis, D.J. Thompson, M.F.M. Hussein. A semi-analytical beam model for the vibration of railway tracks. *Journal of Sound and Vibration* 2017; 393: 321–337.

20   D.J. Thompson. Wheel-rail noise generation, part III: rail vibration. *Journal of Sound and Vibration* 1993; 161: 421-446.

21   K.L. Knothe, Z. Strzyzakowski, K. Willner. Rail vibrations in the high frequency range. *Journal of Sound and Vibration* 1994; 169: 111–123.

22   J. Ryue, D.J. Thompson, P.R. White, D.R. Thompson. Investigations of propagating wave types in railway tracks at high frequencies. *Journal of Sound and Vibration* 2008; 315: 157–175.

23   C.M. Nilsson, C.J.C. Jones, D.J. Thompson, J. Ryue. A waveguide finite element and boundary element approach to calculating the sound radiated by railway and tram rails. *Journal of Sound and Vibration* 2009; 321: 813–836.

24   W. Li, R.A. Dwight, T. Zhang. On the study of vibration of a supported railway rail using the semi-analytical finite element method. *Journal of Sound and Vibration* 2015; 345: 121-145.

25   L. Gry. Dynamic modelling of railway track based on wave propagation. *Journal of Sound and Vibration* 1996; 195: 477-505.

26   X. Zhang, D.J. Thompson, Q. Li, D. Kostovasilis, M.G.R. Toward, G. Squicciarini, J. Ryue. A model of a discretely supported railway track based on a 2.5D finite element approach. *Journal of Sound and Vibration* 2019; 438: 153-174.

27   S.L. Grassie, S.J. Cox. The dynamic response of railway track with flexible sleeper to high frequency vertical excitation. *Proceedings of the Institution of Mechanical Engineers. Part D: Journal of Automobile Engineering* 1984; 198: 117-124.

28   J.C.O. Nielsen, A. Igeland. Vertical dynamic interaction between train and track-influence of wheel and track imperfections. *Journal of Sound and Vibration* 1995; 187: 825-839.

29   S.L. Grassie. Dynamic modelling of concrete railway sleepers. *Journal of Sound and Vibration* 1995; 187: 799-813.

30   M. Oregui, Z. Li, R. Dollevoet. An investigation into the vertical dynamics of tracks with monoblock sleepers with a 3D finite-element model. *Proceedings of the Institution of Mechanical Engineers, Part F: Journal of Rail Rapid Transit* 2016; 230: 891-908.

31   D. Kostovasilis. *Analytical Modelling of the Vibration of Railway Track*, PhD thesis, University of Southampton, UK, 2017.

32   C.J.C. Jones, D.J. Thompson, R.J. Diehl. The use of decay rates to analyse the performance of railway track in rolling noise generation. *Journal of Sound and Vibration* 2006; 293: 485–495.

33 BS EN 15461:2008 A1:2010: Railway applications – Noise emission - Characterization of the dynamic properties of track selections for pass by noise measurements, British Standards Institution, 2010.